Earth's core internal dynamics 1840–2010 imaged by inverse geodynamo modelling

Julien Aubert

Earth's core internal dynamics 1840–2010 imaged by inverse geodynamo modelling

Julien Aubert

Dynamique des Fluides Géologiques, Institut de Physique du Globe de Paris, Sorbonne Paris Cité, Université Paris-Diderot, UMR 7154 CNRS, 1 rue Jussieu, F-75005 Paris, France. E-mail: aubert@ipgp.fr

SUMMARY

Inverse geodynamo modelling seeks to estimate the dynamic state of Earth's core from geomagnetic data and the statistical information brought by a prior self-consistent, 3-D numerical model of the geodynamo. The method rests on the use of least-squares inversions under constraints and estimates hidden quantities by taking advantage of linear relations and long-range statistical correlations with the magnetic observations. The data, together with their error statistics, are provided by geomagnetic field models COV-OBS, gufm-sat-Q3 and CM4, covering epochs 1840–2010. The prior numerical model is the recently published coupled Earth dynamo, the output of which presents a high degree of morphological semblance to the geomagnetic field while reproducing the main features of its secular variation. An analysis of the inversion misfits to the data shows that the prior model generally accounts well for the main field and secular variation data within their specified errors, throughout the investigated time period. Inverted core flows are confirmed to be mainly organized in columns parallel to the Earth's rotation axis. A previously observed giant eccentric columnar gyre of westward-drifting flow is found to be present from epoch 1870 onwards, and its structure is shown to slowly rotate westwards at a rate up to $0.1^\circ \ \mathrm{yr}^{-1}$, confirming an earlier prediction based on direct numerical modelling. Temporal variations in the axisymmetric part of the gyre accurately account for observed variations of the length of the day in recent epochs. Inverted magnetic structures support a mechanism of azimuthal flux expulsion by convective columns to explain the origin of low-latitude magnetic flux patches existing beneath the Atlantic. The 1840–2010 time average of the inverted density anomaly field has a longitudinal hemispheric structure, with most of the buoyancy in the Eastern hemisphere, consistent with rapid surges of convective columns imaged in this hemisphere, with earlier proposals of a faster inner core freezing there, and with a possible east-to-west convective translation of the solid inner core. The typical timescales of flow variation observed in the inversions are two to three times shorter than those naturally produced by a direct simulation of the prior model, underlining its limits in fully rendering the Earth's core short timescale dynamics.

Key words: Inverse theory; Dynamo: theories and simulations; Rapid time variations.

1 INTRODUCTION

In the past decades, global, continuous vector measurements from low orbit satellites have complemented ground-based observatory measurements to significantly increase our knowledge of Earth's magnetic field. The available wealth of satellite and observatory data now permits to construct parametrized field models (recently: Lesur *et al.* 2010; Olsen *et al.* 2010; Finlay *et al.* 2012; Gillet *et al.* 2013) specifically targeted at the study of the convective dynamo operating in Earth's liquid core, which is responsible for the magnetic field of internal origin. To that end, specific strategies include data selection and re-sampling for homo-geneous spatial coverage, subtraction of estimates for the crustal and magnetospheric fields prior to modelling (instead of treating them as sources of error), reduction of the spatial and temporal regularization to minimal levels compatible with theoretical expectations on core dynamics. Core field models constructed for the last 10 yr are now able to resolve main field and secular variation (main field rate-of-change) structures with 1500-km lateral extent at the core–mantle boundary (spherical harmonic degree 13), and with a temporal resolution on the order of a year. It should be noted though that degrees 11–13 are more sensitive to modelling and regularization choices than lower degrees (Finlay *et al.* 2012). In connection with this last point, it is generally quite difficult to provide a reliable

Table 1. Numerical dynamo models used to produce the inversion priors. The two models have the same classical fundamental control parameters (Rayleigh, Ekman, Prandtl, magnetic Prandtl number, inner core and outer core buoyancy heterogeneity amplitudes, amplitude of gravitational coupling, see Aubert *et al.* 2013). Presented here are numbers involving several important timescales of the problem: the magnetic Reynolds number *Rm*, magnetic Ekman number E_η and Alfvén number A. Timescales are the magnetic diffusion timescale $\tau_\eta = D^2/\eta$ (η is the magnetic diffusivity), core overturn timescale $\tau_U = D/U$ (U is the root mean square core velocity), inverse rotation rate $\tau_\Omega = 1/\Omega$ and Alfvén timescale $\tau_A = D(\rho\mu_0)^{1/2}/B$ (ρ, μ_0 and B are, respectively, the core density, vacuum magnetic permeability and typical core magnetic field).

	$Rm = \frac{\tau_\eta}{\tau_U}$	$E_\eta = \frac{\tau_\Omega}{\tau_\eta}$	$A = \frac{\tau_A}{\tau_U}$	Notes
CE	942	$1.2\ 10^{-5}$	0.76	Coupled Earth dynamo (Aubert *et al.* 2013)
G	982	$1.2\ 10^{-5}$	0.87	Thermochemical boundary coupling is removed from CE to obtain G.
Earth's core	900–2000	1–$3\ 10^{-9}$	1–$3\ 10^{-2}$	From values in Aubert *et al.* (2009, 2013)

specification of model uncertainties through the computation of posterior model covariance matrices (Lowes & Olsen 2004). A recent strategy (Gillet *et al.* 2013) attempts to overcome this difficulty by producing an ensemble of models following a stochastic process defined by a prior time covariance function. Obtaining reliable posterior covariance statistics is certainly desirable because the uncertainty associated with each field coefficient, together with possible error cross-correlations, can then in principle be properly accounted for in subsequent geodynamic analyses.

Numerical modelling of core dynamics has recently reached a stage where it can take advantage of the extra information contained in these new geomagnetic field models. Systematic parameter space exploration (Christensen *et al.* 2010) has revealed that the morphology of the output from numerical dynamo simulations can be very similar to the geomagnetic field if three timescales relevant to core dynamics are brought in reasonable proportions relative to their Earth counterparts: the timescales for the advection τ_U, diffusion of the magnetic field τ_η and the core inverse rotation rate τ_Ω (see Table 1 for typical ratios in the models and in the core). For models satisfying this condition, the output secular variation (Lhuillier *et al.* 2011b) and acceleration (Christensen *et al.* 2012) timescales also compare very favourably between the models and the Earth, suggesting that the large-scale kinematics and dynamics of the field are realistically simulated, despite the very unrealistic rendering of the underlying small-scale fluid flow turbulence (see Christensen 2011 for a review). Until recently however, this success needed to be contrasted by acknowledging that the detailed morphological agreement between snapshots of the model and Earth secular variation was worse than that between snapshots of the model and Earth magnetic field itself (Aubert *et al.* 2013).

Our recent work has focused on inverse modelling and data assimilation techniques (see Fournier *et al.* 2010 for a review) providing tools to quantify and interpret such discrepancies. Inverse geodynamo modelling (Aubert 2013) images a fluid flow throughout the core that accounts for the geomagnetic secular variation, while being statistically compliant with a numerical dynamo used as a prior model. It is an inverse technique, but also a modelling technique because it can guide modelling choices in the following way: a posterior assessment of the flow solution against the statistical behaviour of the numerical dynamo enables identification of the shortcomings of the prior model; further modelling improvements can then be evaluated against this benchmark. This strategy led us to refine the existing dynamo models by including realistic mechanical and thermochemical couplings between the Earth's outer core,

inner core and mantle. The resulting coupled Earth dynamo model (Aubert *et al.* 2013) successfully reproduces the details of Earth's magnetic field and secular variation up to the spatial resolution available in geomagnetic field models. The model also highlights mechanisms potentially responsible for the previously observed peculiar morphology of the deep core flow (Pais & Jault 2008; Gillet *et al.* 2009; Aubert 2013).

This study aims at advancing inverse geodynamo modelling in the light of the recent progress made by geomagnetic field models and numerical simulations. Areas of improvement over Aubert (2013) are the following: (i) The framework is expanded in order to include inversions for the internal magnetic and density anomaly fields, in addition to the velocity field. (ii) The coupled Earth dynamo model is used as a prior for the inversion, in order to best account for the geomagnetic signal. (iii) The geomagnetic field model COV-OBS is used in addition to models CM4 (Sabaka *et al.* 2004) and gufm-sat-Q3 used previously. The posterior model covariance matrices specified in COV-OBS can readily be used as prior data error covariance matrices in the inverse geodynamo modelling framework. (iv) Unknown sources affecting the secular variation signal (the magnetic field and flow underparametrization, and magnetic diffusion in Aubert 2013) are explicitly estimated and removed from the data prior to core flow inversion, instead of being treated as errors. The updated framework enables investigation of the core dynamic state between epochs 1840 and 2010, roughly covering a convective overturn of the core. This interval is appropriate for a detailed analysis of the dynamics retrieved from the inverted core states, and enables an assessment of the ability of current numerical simulations to render this dynamics. Section 2 describes the numerical dynamo models, geomagnetic field models and the inversion technique. Section 3 presents the results, which are then discussed in Section 4.

2 MODELS AND METHODS

2.1 Self-consistent models of core dynamics

The numerical dynamo model solves for Boussinesq convection and magnetic induction in the magnetohydrodynamic approximation in a spherical fluid shell between radii r_{ICB} and r_{CMB}, with the present Earth's core aspect ratio $r_{ICB}/r_{CMB} = 0.35$, which is coupled to an electrically conducting solid inner core of radius r_{ICB} and to an insulating mantle shell between radii r_{CMB} and $1.83r_{CMB}$. The whole

system has a constant solid-body rotation rate Ω defining the planetary rotating frame. As mentioned in Section 1, the precise model setup is described in Aubert *et al.* (2013), and details on the model equations, numerical implementation, definitions and values for the dimensionless parameters can be found in Aubert *et al.* (2009) and Aubert & Dumberry (2011). Two configurations are used (Table 1). The coupled Earth dynamo (termed CE in the following) favours indirect coupling between the outer core and the mantle, via the inner core, over direct coupling through the core–mantle boundary. Practically, this amounts to specifying no-slip and electrically conducting boundary conditions at the inner core boundary, free-slip and insulating boundary conditions at the core–mantle boundary, and a gravitational torque remotely coupling the axially rotating mantle and inner core. This configuration localizes strong westward outer core thermochemical winds below the core–mantle boundary, and the resulting magnetic field kinematics account for the main properties of the historical geomagnetic westward drift (Jackson *et al.* 2000; Finlay & Jackson 2003). Heterogeneous mass anomaly flux boundary conditions are also adopted at both boundaries of the outer core. The outer boundary condition models the effects of thermal control from the lower mantle, while the inner condition models the effects of thermochemical buoyancy release associated with a longitudinal hemispheric modulation in inner core growth rate. The ratio between the peak-to-peak inner boundary mass anomaly flux heterogeneity and the mean flux is 0.8, corresponding to a differential inner core growth rather than a complete translation of inner core material as initially proposed by Alboussière *et al.* (2010) and Monnereau *et al.* (2010). The maximum of inner core buoyancy release is set at 90°E, consistently with the expected effects of thermal forcing from the mantle (Aubert *et al.* 2008). In addition to the CE model, model G from Aubert *et al.* (2013) is also used. This model retains indirect core–mantle inner core mechanical coupling but does not implement heterogeneous thermochemical control from the inner and outer core boundaries.

The dynamo models supply the core magnetic, density anomaly and velocity fields in dimensionless forms. Re-scaling these quantities into the dimensional world is an obligatory step for inversion and data assimilation. Canonical physical units cannot be used entirely in this step, owing to the large parameter space gap between the numerical models and the Earth's core. The approach followed in earlier studies (Aubert & Fournier 2011; Aubert 2013) is rather to rationalize this parameter gap by using units underlain by scaling principles thought to hold in both the model and the Earth's core. The canonical length unit is used, the

non-dimensional shell gap $D = r_{CMB} - r_{ICB}$ being assigned the value 2260 km. The non-dimensional secular variation timescale τ_{sv} of the model is assigned the Earth dimensional value 415 yr (Lhuillier *et al.* 2011b), meaning that the physical time is obtained by multiplying the non-dimensional model time with 415 yr and dividing by the model non-dimensional value of τ_{sv}. Likewise, the non-dimensional, convective-power based scaling prediction (Christensen & Aubert 2006) for the magnetic field amplitude in the models is adjusted to the dimensional value $[B] = (\rho \mu_0^3 p^2 D^2)^{1/6}$, where $\rho = 11\,000\,\mathrm{kg\,m^{-3}}$, μ_0 and p are, respectively, the density, vacuum magnetic permeability and convective power density in the outer core. Finally, the density anomaly unit is set by matching the non-dimensional model value of $[C] = p\tau_{sv}/g_{CMB}D$, where $g_{CMB} = 10\,\mathrm{m\,s^{-2}}$ is the gravity at the core–mantle boundary, to its value in the Earth's core. The convective power density p is obtained by assuming that heat flow at the Earth's core–mantle boundary is presently exactly adiabatic, with a value $Q_{ad} = 15\,\mathrm{TW}$ (Pozzo *et al.* 2012), and that the core does not contain radioactive elements (note that the distribution of mass anomaly fluxes in the CE dynamo is consistent with these choices). The present-day thermodynamic efficiency of the geodynamo is then $\epsilon = 0.2$ (Aubert *et al.* 2009), and the total geodynamo convective power is $\epsilon Q_{ad} = 3\,\mathrm{TW}$, corresponding to a power density $p = 1.78\,10^{-8}\,\mathrm{W\,m^{-3}}$. From this, follow the values $[B] = 1.81\,\mathrm{mT}$ and $[C] = 1.03\,10^{-5}\,\mathrm{kg\,m^{-3}}$. It should be noted that variations in p weakly influence the magnetic field scale, as p enters the definition of $[B]$ only to the power 1/3. The inversion results are thus generally robust when a range of possible present core thermodynamic states (Pozzo *et al.* 2012) is considered, except for the density anomaly results which need to be rescaled accordingly. Likewise, the uncertainty of ± 50 yr reported on the secular variation timescale (Lhuillier *et al.* 2011b) also only weakly influences the inversion, as it mostly modifies the non-dimensional secular variation data, but later cancels this modification when the non-dimensional velocity field is cast back to the dimensional world.

2.2 Parametrized models of the geomagnetic field evolution

A list of the geomagnetic field models analysed here is shown in Table 2. The spline expansion for all models permits the computation of the secular variation or first time derivative of the main field, which is the highest derivation order considered here. In the inversions presented in Section 3, the field and its secular variation are

Table 2. Parametrized models of the geomagnetic field evolution. Data from all models are retained up to spherical harmonic degree and order 13, both for the field B and its secular variation $\dot{B}$. For models CM4 and gufm-sat-Q3 with unspecified error statistics, the error is evenly distributed across spherical harmonic degrees, corresponding to flat Mauersberger–Lowes spectra at the Earth's surface. The last column reports the integral rms error at the Earth's surface, which is set consistently with the error observed in COV-OBS at similar epochs.

Model	Time span	Spline order	Knot spacing	Regularization / prior	Error model
COV-OBS (Gillet *et al.* 2013)	1840–2010	4	2 yr	AR2 stochastic temporal process with satellite-era variances	Supplied single-epoch posterior covariance matrices
CM4 (Sabaka *et al.* 2004)	1960–2000	4	2.5 yr	Squared surface Laplacian in space, second-order time derivative (core–mantle boundary)	B: 2 nT, $\dot{B}$: 2 nT yr^{-1}
gufm-sat-Q3 (Finlay *et al.* 2012)	2000–2010	6	0.25 yr	Quadratic in space, third-order time derivative (core–mantle boundary)	B: 1 nT, $\dot{B}$: 1 nT yr^{-1}

considered at discrete single epochs corresponding to nodal points in their spline expansions, and retained up to spherical harmonic degree and order 13. The ensemble of models provided by COV-OBS enables computation of posterior covariance matrices for the field and secular variation coefficients (Gillet *et al.* 2013). These are extracted at nodal single epochs for use in the inversion framework as prior error covariance matrices. In the case of gufm-sat-Q3 and CM4, which are not supplied with an error model, the errors of individual field and secular variation coefficients are evenly distributed among spherical harmonic coefficients in such a way that they correspond to flat energy spectra at the Earth surface (similarly to Aubert 2013, see levels in Table 2). Errors on different field coefficients are additionally assumed to be independent, yielding a diagonal error covariance matrix.

Most of the results presented here are obtained with COV-OBS, because of its large time span and modelling assumptions specifically targeted at the study of core dynamics. However, as the temporal resolution of this model is quite coarse in the satellite era, the high temporal resolution of gufm-sat-Q3 is also a benefit. More generally, it is instructive to interpret and assess the robustness of the results obtained here in the light of the different regularization, modelling and error model choices adopted in CM4, gufm-sat-Q3 and COV-OBS. Indeed model COV-OBS is constructed using regularization which may arguably be seen as weaker than those adopted for gufm-sat-Q3 and CM4. The spatial regularization of these latter models is of quadratic type (but they penalize different derivation orders in space), while COV-OBS only specifies a prior individual variances for the Gauss coefficients following prescriptions from the gufm-sat series of models. The temporal regularization is CM4 and gufm-sat-Q3 are prescribed by penalizing the second and third derivative of the magnetic field, respectively, while COV-OBS represents an ensemble of stochastically generated field models satisfying an *a priori* specified time correlation function, in this case an autoregressive, order 2 (AR2) process. This approach yields typical Earth surface secular acceleration (second field time derivative) energies twice stronger in COV-OBS than in the other models. The inverse geodynamo modelling results presented in Section 3 provide elements to discuss the realism of the resulting COV-OBS error covariance matrices.

2.3 Inverse geodynamo modelling framework

The implementation of inverse geodynamo modelling follows on the concepts introduced in Aubert & Fournier (2011) and Aubert (2013). The principle is to seek the most likely core state (in the least-squares sense) accounting for the core field and secular variation data, while being statistically compliant with the output of a numerical model of the geodynamo. The retrieval of a full core state from surface data is performed by taking advantage both of physical laws linearly connecting observed and unobserved quantities of the system, and of long-range statistical correlations existing between these quantities (see Aubert & Fournier 2011 for a detailed discussion of the nature of these correlations).

2.3.1 Numerical geodynamo statistics

Multivariate statistics are first extracted from the three models CE and G. For each model, a preliminary numerical run of the model is performed and $n = 800$ complete snapshots of the model state are stored, the spacing between each snapshot being set to 100 yr. This is three times larger than the typical e-folding time (Lhuillier

et al. 2011a) of these models, which is about 30 yr, thus ensuring statistical decorrelation of the snapshots. A complete model state vector at time t_i writes (superscript Tr denotes the transpose)

$$\mathbf{x}(t_i) = [S_{lm}(r_j, t_i), T_{lm}(r_j, t_i), W_{lm}(r_j, t_i),$$
$$Z_{lm}(r_j, t_i), C_{lm}(r_j, t_i)]^{\mathrm{Tr}}, \tag{1}$$

and contains the complex values of the spheroidal and toroidal components S and T of the velocity field $\mathbf{u}$, the poloidal and toroidal components W and Z of the magnetic field $\mathbf{B}$ and the convective density anomaly field C, for each harmonic degree and order l, m on the nodes j of the radial grid used by the numerical implementation. In the following, all fields in the state vector are statistically centred by removing their corresponding time average computed over the preliminary run, and normalized to unit variance by dividing them with the standard deviation computed over the preliminary run. For reasons of computational efficiency, and because the data available up to spherical harmonic degree and order 13 cannot reliably constrain a very high-resolution core state (Aubert & Fournier 2011), the state vector is truncated at spherical harmonic degree and order 30 (the maximum degree is 133 in the numerical simulation). The full extent of the radial resolution of the numerical computation is however retained, amounting to 160 radial levels in the outer core and 25 radial levels in the inner core.

A magnetic state vector is defined as

$$\mathbf{x}_B(t_i) = [W_{lm}(r_j, t_i), Z_{lm}(r_j, t_i)]^{\mathrm{Tr}}_{0 \le r_j \le r_{\mathrm{CMB}}, l \le 30}. \tag{2}$$

Note that the magnetic field inside the electrically conducting inner core is included in the state vector. The corresponding covariance matrix is computed using

$$\mathbf{X}_B = [\mathbf{x}_B(t_1), \mathbf{x}_B(t_2), \ldots, \mathbf{x}_B(t_n)],$$
$$\mathbf{P}_B = \frac{1}{n-1} \mathbf{X}_B \mathbf{X}_B{}', \tag{3}$$

where the prime denotes the transpose complex conjugate. Following the same procedure, a core surface velocity state vector is defined as $\mathbf{x}_{fs}(t_i) = [S_{lm}(r_{\mathrm{CMB}}, t_i), T_{lm}(r_{\mathrm{CMB}}, t_i)]^{\mathrm{Tr}}_{l \le 30}$ and the corresponding covariance matrix $\mathbf{P}_{fs}$ is computed (see fig. 3 in Aubert 2013 for a graphical representation). Note that the dynamo models use a free-slip boundary condition at the outer boundary; the free stream is thus exactly located at radius r_{CMB}. A full velocity state vector is also defined as

$$\mathbf{x}_u(t_i) = [S_{lm}(r_j, t_i), T_{lm}(r_j, t_i)]^{\mathrm{Tr}}_{r_{\mathrm{ICB}} \le r_j \le r_{\mathrm{CMB}}, l \le 30}, \tag{4}$$

with its corresponding covariance matrix $\mathbf{P}_u$. Finally, a density anomaly state vector augmented with the core surface flow velocity is introduced as

$$\mathbf{x}_C(t_i) = [C_{lm}(r_j, t_i), S_{lm}(r_{\mathrm{CMB}}, t_i),$$
$$T_{lm}(r_{\mathrm{CMB}}, t_i)]^{\mathrm{Tr}}_{r_{\mathrm{ICB}} \le r_j \le r_{\mathrm{CMB}}, l \le 30}, \tag{5}$$

with the corresponding covariance matrix $\mathbf{P}_C$. Augmenting this last state vector enables a simple formulation for the density anomaly direct problem (see eq. 13).

2.3.2 Inversion procedure

A data vector $\mathbf{b} = [B^p_{lm}(r_{\mathrm{CMB}})]^{\mathrm{Tr}}_{l \le 13}$ is first constructed and contains the core surface poloidal main field output from a geomagnetic field model. The data vector is then transformed in the same way as described above, that is, by removing the mean and normalizing by the standard deviation of the corresponding dynamo model field over the preliminary run. The inversion first estimates the magnetic

field throughout the core up to degree and order 30 from the surface poloidal magnetic field data up to degree and order 13, and the statistics provided by $\mathbf{P}_B$. The direct problem writes

$$\mathbf{H}_B \mathbf{x}_B = \mathbf{b}. \tag{6}$$

The operator $\mathbf{H}_B$ bears the classical form of observation operators used in this context (see, e.g. eq. 22 in Aubert 2013), consisting of entries equal to 1 when the quantity is observed and zeros otherwise. The best linear inverse (also called stochastic inverse, Aubert & Fournier 2011; Fournier *et al.* 2011) is expressed as

$$\mathbf{x}_B = \mathbf{P}_B \mathbf{H}_B'(\mathbf{H}_B \mathbf{P}_B \mathbf{H}_B' + \mathbf{R}_B)^{-1}\mathbf{b}, \tag{7}$$

where $\mathbf{R}_B$ is the error covariance matrix on surface magnetic field coefficients, as supplied by model COV-OBS, or as prescribed *a priori* for other geomagnetic field models (see Table 2). Note that this step purely relies on the long-range statistical correlations existing in the model between the surface and deep magnetic fields. Note also that it enables estimation of the small-scale part of the surface magnetic field (between harmonic degrees 14 and 30) by relying on the correlations existing in the spectral space between different harmonic degrees at the same harmonic order of the surface magnetic field (see Aubert & Fournier 2011 for a detailed description). In the real space, these correlations translate into core surface magnetic flux patches generally elongated in the latitudinal direction. Note also that this step permits to compute an estimate of magnetic diffusion at the core surface, since the radial derivatives of the radial magnetic field are accessible. Typical estimations of magnetic diffusion and small-scale magnetic field are illustrated in fig. 4 of Aubert (2013).

The second step is an inversion of the magnetic induction equation at the core surface. This equation writes

$$\frac{\partial \mathbf{B}}{\partial t} = \nabla \times (\mathbf{u} \times \mathbf{B}) + \eta \nabla^2 \mathbf{B}. \tag{8}$$

Here, η is the magnetic diffusivity of the core fluid. At each single epoch, eq. (8) is linearized to yield the direct problem for the core surface flow:

$$\mathbf{M}\mathbf{x}_{fs} = \dot{\mathbf{b}} + \mathbf{c}. \tag{9}$$

Here, $\dot{\mathbf{b}} = [\partial B_{lm}^p(r_{\mathrm{CMB}})/\partial t - \eta \nabla^2 W_{lm}(r_{\mathrm{CMB}})]_{l \leq 13}^{\mathrm{Tr}}$ is the vector containing the core surface poloidal secular variation output from a geomagnetic field model, corrected with the above estimate of core surface magnetic diffusion, and again normalized using the standard deviations from the numerical dynamo model. The matrix $\mathbf{M}$ contains the Elsasser and Adams-Gaunt coupling integrals (see section 2.2.1 in Aubert 2013 for details) between unknown flow coefficients, and known field coefficients, up to degree and order 30. The core surface magnetic field coefficients used in $\mathbf{M}$ are the output of the previous step (eq. 7), following the data within the specified error if the degree is less or equal than 13, and entirely resulting from the previous inversion if the degree is between 14 and 30. The vector $\mathbf{c}$ arises in the formulation because $\mathbf{x}_{fs}$ is statistically centred. It contains the product of $\mathbf{M}$ with the time average of $\mathbf{x}_{fs}$ over the dynamo model preliminary run (this vector is present in eq. 10 below but omitted afterwards for simplicity). The best linear inverse is

$$\mathbf{x}_{fs} = \mathbf{P}_{fs}\mathbf{M}'(\mathbf{M}\mathbf{P}_{fs}\mathbf{M}' + \mathbf{R}_{\dot{B}})^{-1}(\dot{\mathbf{b}} + \mathbf{c}). \tag{10}$$

Here, $\mathbf{R}_{\dot{B}}$ is the error covariance matrix on surface secular variation coefficients, as supplied by model COV-OBS, or as prescribed *a priori* for other geomagnetic field models (see again Table 2). This step thus combines the knowledge of a physical law connecting the core surface magnetic field, secular variation, and velocity field, together with statistical knowledge used to reduce the non-uniqueness of the solution to the direct problem (9). The explicit estimation of magnetic diffusion and underparametrization enable a single-pass inversion at this step, a practical improvement over Aubert (2013) where the inversion was iterative.

The third step is the retrieval of the velocity field throughout the core. Here, again the scheme takes advantage of the long-range correlations existing between surface and deep flow, owing to the leading influence of the Coriolis force, and giving rise to a columnar organization of the flow on timescales much shorter than the ones considered here (Jault 2008). The direct problem writes

$$\mathbf{H}_u \mathbf{x}_u = \mathbf{x}_{fs}, \tag{11}$$

where $\mathbf{H}_u$ is a flow observation operator (eq. 22 in Aubert 2013), similar in form to $\mathbf{H}_B$. The best linear inverse is

$$\mathbf{x}_u = \mathbf{P}_u \mathbf{H}_u'(\mathbf{H}_u \mathbf{P}_u \mathbf{H}_u')^{-1}\mathbf{x}_{fs}. \tag{12}$$

In the final step, the time-average density anomaly field throughout the core is estimated by assuming long-range correlation with and linear dependency on the time-average core surface velocity field. The rationale underlying these assumption is based on the existence of a thermochemical wind balance (e.g. Aubert 2005) linearly connecting the density anomaly field to the velocity field, and on the strong correlations (already invoked above) existing between the deep and surface velocity fields. If $\overline{\mathbf{x}_{fs}}$ denotes a time-average velocity field obtained with the previous inversion procedure repeated throughout the time span of a geomagnetic field model, then the direct problem for the time-averaged augmented state vector $\overline{\mathbf{x}_C}$ is formulated as

$$\mathbf{H}_C \overline{\mathbf{x}_C} = \overline{\mathbf{x}_{fs}}. \tag{13}$$

The observation operator $\mathbf{H}_C$ is again a sparse matrix similar in form to $\mathbf{H}_B$ or $\mathbf{H}_u$. The best linear inverse is

$$\overline{\mathbf{x}_C} = \mathbf{P}_C \mathbf{H}_C'(\mathbf{H}_C \mathbf{P}_C \mathbf{H}_C')^{-1}\overline{\mathbf{x}_{fs}}. \tag{14}$$

In the present inversions, the trade-off between fit to the data and spatial complexity is not controlled by damping norms of adjustable strength, but rather by compliance to the covariance matrices supplied by the numerical dynamo prior. Furthermore, the inversions are taken at single epochs corresponding to nodal points of the geomagnetic field models spline expansions. In that sense the temporal regularity of the sequence of inverted states is then controlled by that of the geomagnetic field model. Avoiding temporal regularization in the inversions also enables an *a posteriori* check where the inverted flow variations are compared to variations typically observed in a free run of the prior numerical model.

The present framework admittedly deals with errors in an optimistic way. The inversion (10) neither accounts for the errors on the main magnetic field (from the geomagnetic field model or the small-scale estimation) built into matrix $\mathbf{M}$, nor does it include the errors on the magnetic diffusion estimation. Note however that including these errors would be equivalent to treating the problem as in Aubert (2013). Likewise, coupling between field and flow at harmonic degrees larger than 30 is not considered in eq. (9) (this presumably has a negligible effect on the determination of flow up to degree 13). The synthetic experiments presented in the next section provide arguments in support of this optimistic error treatment. Furthermore, the chain of inversions (10,12,14) would require propagation of the posterior errors of former problems as prior errors in latter problems. This has not been done here for simplicity and will be implemented in a future step.

Table 3. Recovery quality of known synthetic core states, evaluated for a sequence of model CE comprising 86 snapshots with 2-yr spacing in time. The inversion scheme uses the statistics of the same model as that used to produce the synthetics (twin experiment). Core-surface magnetic field and secular variation data are extracted up to spherical harmonic degree and order 13. The error model adopted for the synthetic data is the same as that adopted for geomagnetic model gufm-sat-Q3 in Table 2. (a) Vector correlation coefficients and pointwise recovery factors (as defined in Amit *et al.* 2007) between the reference core surface velocity field and the field recovered using the inversion scheme. Also reported are the normalized prior and posterior misfits $\Delta_{\dot{B}}$ and Δ_{fs} (see text for definitions). The reported values are averages over the 86 realizations of the twin experiment. See table 2, second experiment in Aubert (2013) for comparison. (b) Vector correlation coefficients computed throughout the core between the reference and recovered fields. Results are averages over the 86 realizations of the twin experiment. For the density anomaly field, the result of a single experiment estimating the 170-yr time-average density anomaly field from the time average of recovered velocity fields is also reported. In order to remove a bias towards optimistic results, the axisymmetric part of the density anomaly field is removed prior to computation of the correlation coefficients.

(a) Recovery of core surface flow snapshots			
Correlation coefficient (degree 30, degree 13)	Pointwise recovery factor (degree 30, degree 13)	$\Delta_{\dot{B}}$	Δ_{fs}
0.51, 0.73	0.47, 0.62	0.85	0.76

(b) Recovery of deep fields		
Field	Time span	Correlation coefficient (degree 30, degree 13)
Density anomaly field C	170-yr average	0.66, 0.73
Velocity field **u**	Snapshots	0.46, 0.64
Magnetic field **B**	Snapshots	0.40, 0.54
Density anomaly field C	Snapshots	0.43, 0.53

2.4 Validation

One can question the ability of the scheme to retrieve, from surface data only, a known synthetic core state obtained with the same numerical model as that used to build $\mathbf{P}_B$, $\mathbf{P}_{fs}$, $\mathbf{P}_u$ and $\mathbf{P}_C$. This forms the basis of 'twin' experiments, the results of which are presented in Table 3. Table 3(a) reproduces the diagnostics presented in table 2 of Aubert (2013). The flow recovery quality is improved with the present scheme, as witnessed by the higher correlation coefficients and pointwise recovery factors. Furthermore, the prior misfit (or normalized data misfit)

$$\Delta_{\dot{B}} = \frac{1}{N_B}\sqrt{\left(\dot{\mathbf{b}} - \mathbf{M}\mathbf{x}_{fs}\right)' \mathbf{R}_{\dot{B}}^{-1} \left(\dot{\mathbf{b}} - \mathbf{M}\mathbf{x}_{fs}\right)}, \tag{15}$$

where $N_B = 195$ is the number of degrees of freedom in the secular variation data expanded up to spherical harmonic degree and order 13, evaluates the quality of the inversion fit to the data (0 is optimal, 1 is statistically acceptable). This fit is markedly better with the present inversion scheme, first because $\Delta_{\dot{B}}$ is lower than in Aubert (2013), and also because the error level entering $\Delta_{\dot{B}}$ is itself also reduced to the sole observational error. Likewise, the posterior misfit

$$\Delta_{fs} = \frac{1}{2N_m}\sqrt{\left(\mathbf{x}_{fs}' \mathbf{P}_{fs}^{-1}\mathbf{x}_{fs}\right)} \tag{16}$$

evaluates how much the inverted flow deviates from the model time average (1 is optimal, 0 is statistically acceptable). Here, $N_m = 960$ is the number of degrees of freedom of each of the two components of the core surface velocity field, expanded up to spherical harmonic degree and order 30. Using the updated inversion scheme, this misfit is brought closer to 1, corresponding to a more energetic inverted flow with better statistical compliance with the inversion prior. In summary, the explicit estimation of the core–mantle boundary small-scale magnetic field and magnetic diffusion in eqs (9) and

(10) appears to bring valuable additional information to the inversion, although their recovery quality is admittedly only of average quality (respective correlation coefficients 0.47 and 0.40).

Turning now to the recovery quality of internal fields (Table 3b), the best result is obtained with a 170-yr time average of the density anomaly field. The recovery of the deep velocity field is satisfactory but inferior to that of the surface velocity field, especially when smaller scales are considered. The recovery of the internal magnetic field is of average quality, an expected result since this inversion solely relies on statistical correlations, in contrast to the robust physical equilibria underlying the recovery of the velocity and time-average density anomaly fields. An average recovery quality is also obtained when one attempts to retrieve density anomaly snapshots instead of time averages using eq. (14). In that case indeed, magnetic and inertial forces perturb the thermochemical wind balance. In that regard, the twin experiment results show that the averaging time of 170 yr available in COV-OBS appears sufficient to mitigate their influence.

One can also question the ability of the scheme to retrieve the actual state of the Earth's core, which is quite remote in parameter space from the numerical model. To address this second concern, it should first be recalled that the determination of the whole core flow relies first on the core surface magnetic induction eq. (9), and then on the leading influence of the Coriolis force. Likewise, the determination of the whole core time-average density anomaly field (eq. 14) relies on the thermochemical wind equilibrium on core overturn timescales. These physical equilibria are expected to hold in a similar manner in the CE dynamo model and in the Earth's core owing to the realistic balances between the buoyancy, Coriolis and magnetic forces maintained in this model at overturn timescales (Aubert *et al.* 2013). In contrast, the determination of the deep magnetic field may be more prone to prior dependency owing to the lack of a clear linear relationship between the surface and deep field.
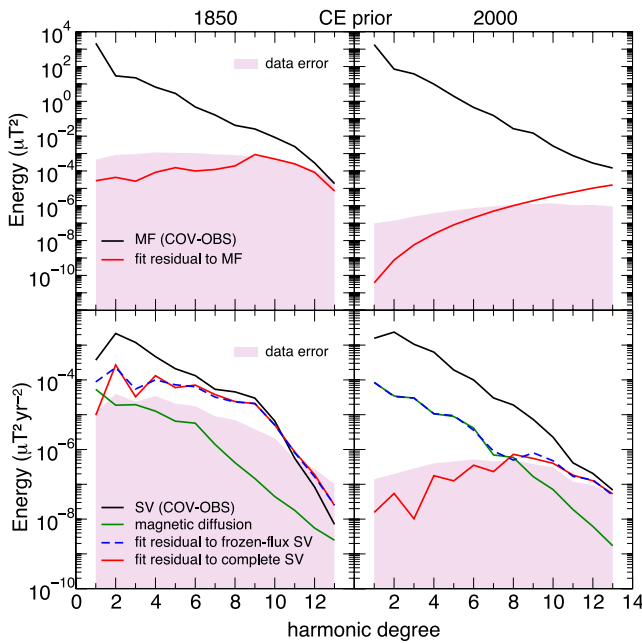
Figure 1. Mauersberger and Lowes energy spectra (black lines) of the main magnetic field (MF, top) and secular variation (SV, bottom) from COV-OBS in 1850 (left-hand side) and 2000 (right-hand side). Also shown are the inversion residuals obtained with prior CE (red lines), together with the typical data error levels (purple zones) prescribed by COV-OBS. These error levels are obtained by summing the diagonal variances in $\mathbf{R}_B$ and $\mathbf{R}_{\dot{B}}$. In the lower panels corresponding to the secular variation, the spectra of the estimated magnetic diffusion $\eta \nabla^2 W_{lm}(r_{\mathrm{CMB}})$ are also reported (green lines), together with the spectra of fit residuals to the secular variation $\mathbf{Mx}_{fs} - \dot{\mathbf{b}}$ (red lines). The frozen-flux misfits to the secular variation data in dashed blue lines then correspond to $\mathbf{Mx}_{fs} - \dot{\mathbf{b}} - \eta [\nabla^2 W_{lm}(r_{\mathrm{CMB}})]_{l \le 13}^{\mathrm{Tr}}$.

3 RESULTS

Fig. 1 presents the fit quality of the inversion to the surface geomagnetic data from COV-OBS at epochs 1850 and 2000. The fit to the surface magnetic field is satisfactory in 1850, with a residue below the data error. The same fit is notably worse in 2000, as the residue exceeds the specified data error after degree 8. Interestingly, the opposite picture is obtained with fits to the secular variation: the fit residue on secular variation data in 1850 exceeds the specified error at large scales (degrees lower than 10), while the fit residue in 2000 lies within the specified error. Further quantification of the fit quality can be obtained in Fig. 2, showing the normalized misfit (or prior misfit) to the secular variation data $\Delta_{\dot{B}}$, together with the corresponding misfit to the magnetic field data Δ_B defined as

$$\Delta_B = \frac{1}{N_B} \sqrt{(\mathbf{b} - \mathbf{H}_B \mathbf{x}_B)' \, \mathbf{R}_B^{-1} \, (\mathbf{b} - \mathbf{H}_B \mathbf{x}_B)}. \tag{17}$$

Here, the core surface poloidal magnetic field data expanded up to spherical harmonic degree and order 13 again have $N_B = 195$ degrees of freedom. The normalized misfit to main field data Δ_B obtained with models G and CE is close to 1 for COV-OBS throughout 1840–2000, indicating a satisfactory fit within the specified errors, and then rapidly increases towards values of about 4. In contrast, in the case of gufm-sat-Q3 and CM4 the normalized misfit indicates close to perfect adjustment of the inverted surface field to the data. This striking difference arises from error cross-correlation between field model coefficients, rather than from the difference between the actual values of these coefficients. Indeed, removing the non-diagonal terms in the matrix $\mathbf{R}_B$ prescribed by COV-OBS yields a fit
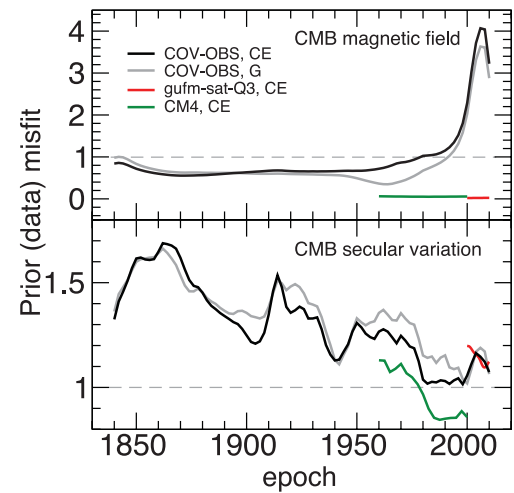
Figure 2. Normalized misfits to the data (prior misfits) Δ_B (top) and $\Delta_{\dot{B}}$ (bottom, see text for definitions), obtained by inverting models COV-OBS, gufm-sat-Q3 and CM4 with priors CE and G. A misfit of 1 (dashed grey line) denotes an acceptable fit (0 is optimal).

to data comparable to the results of gufm-sat-Q3 and CM4, both of which use a diagonal error covariance matrix. Conversely, adopting the COV-OBS error statistics for the inversion of gufm-sat-Q3 or CM4 yields results similar to those obtained with COV-OBS.

The misfit to the secular variation $\Delta_{\dot{B}}$ decreases in an oscillatory manner from values of about 1.5 in 1840 to values close to 1 in 2010. In the general situation of a model with some level of incompatibility with the data, a decreasing level of data error (as specified by COV-OBS as time advances) should yield increasing data misfits. The fact that the opposite long-term trend is observed is encouraging, because it shows that the CE dynamo model secular variation is compatible with the most reliable (most recent) part of COV-OBS. It also suggests that while the secular variation errors specified for the most recent part of COV-OBS appear to be appropriate, the error specification for the earliest epochs may be optimistic. Turning to the decadal oscillations in $\Delta_{\dot{B}}$, the local misfit peaks are caused by known rapid surges in the secular variation energy at the Earth surface (see, e.g. fig. 26 in Jackson & Finlay 2007), which is where the data errors are specified. An examination of COV-OBS indeed yields local maxima in Earth surface secular variation energy at epochs 1868, 1914, 1950, 1978 and 2010, which roughly coincide with the peaks obtained in $\Delta_{\dot{B}}$. Finally, comparing the quality of fits to the main field and its secular variation, it appears that the latter is notably better than the former in the satellite era (2000–2010). This is another hint that error cross-correlations in the COV-OBS main field are optimistic in this era.

Fig. 3 illustrates the temporal evolution of the fit to individual secular variation Gauss coefficients. Consistent with Fig. 2, the fit to secular variation data at all scales is not optimal at the beginning of the observatory era, and later improves. Between 1960 and 2000, large scales of the secular variation appear to tightly follow the data, while smaller scales such as g_{10}^5 appear to be more driven by the prior model, owing to the large uncertainty specified for these coefficients. In that case, the fitted evolution shows weaker variability against the choice of input geomagnetic field model.

Fig. 4 presents a statistical evaluation of the prior model ability to produce the state required by the data. The most relevant fields for this analysis are the core–mantle boundary magnetic field and fluid flow, as they sit closest to where the data are available. The evaluation is best formalized using the normalized deviation to model time
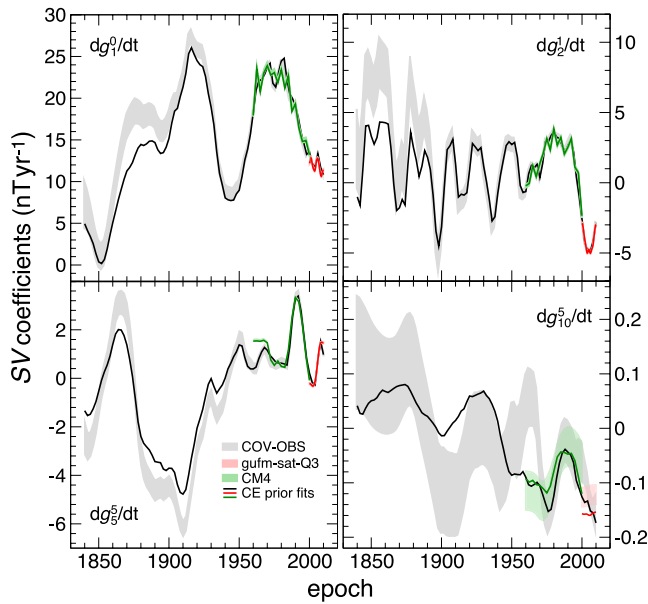
Figure 3. Time derivatives of the geomagnetic potential Gauss coefficients g_l^m (as defined, e.g. in Finlay *et al.* 2010b). Shaded regions represent the $\pm 1\sigma$ error range of the geomagnetic field models, and solid curves indicate the inversion fit to these models. See also fig. 5 in Gillet *et al.* (2013) for comparison.
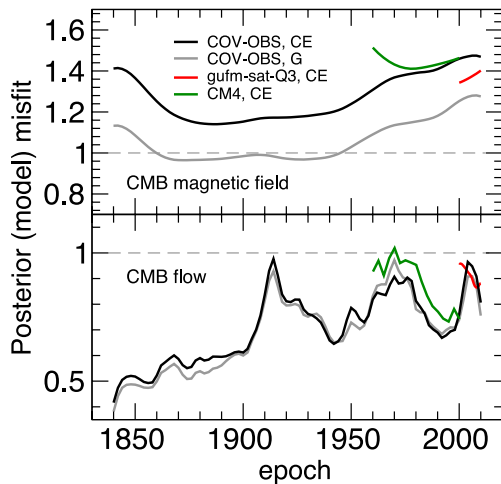

Figure 4. Normalized deviations to model time average (posterior misfits) Δ_m (top) and Δ_{fs} (bottom, see text for definitions), obtained by inverting models COV-OBS, gufm-sat-Q3 and CM4 with priors CE and G. A misfit of 1 (dashed grey line) denotes an optimal energy for the inverted state.

average (or posterior misfit) Δ_{fs}, together with the corresponding quantity for the main magnetic field

$$\Delta_m = \frac{1}{N_m}\sqrt{\left(\mathbf{x}_B'\mathbf{P}_B^{-1}\mathbf{x}_B\right)_{r_{\text{CMB}}}}. \qquad (18)$$

Here, the core–mantle-boundary poloidal field coefficients expanded up to spherical harmonic degree and order 30 have $N_m = 960$ degrees of freedom. The posterior misfit Δ_m remains close to unity throughout 1840–2010, and Δ_{fs} increases towards unity in an oscillatory manner reminiscent of Fig. 2. This generally denotes statistical compliance between the model output and the state required by the data, with best results obtained in recent epochs where the data error is lowest.
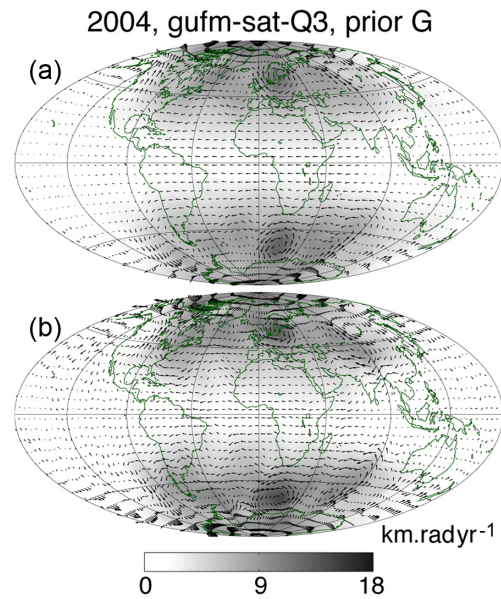
Figure 5. Core surface flow (arrows, arbitrary scaling), superimposed on a grey-scale map of the toroidal velocity scalar $T(r_{\text{CMB}})$ measuring the amount of local surface rotation, inverted in 2004 from model gufm-sat-Q3 and prior G, using (a) the inversion procedure from Aubert (2013) which treats underparametrization and magnetic diffusion as sources of error, and (b) the present inversion procedure which explicitly estimates their contributions.

The updated core surface flow inversion procedure explicitly computes the effects of magnetic diffusion and underparametrization (eqs 9,10 and associated discussion) instead of treating them as sources of error, as previously done in Aubert (2013). Fig. 5 compares the core surface flows obtained with the two approaches, using the same data and numerical prior. The normalized data misfits are similar, $\Delta_{\dot{B}} = 1.17$ for the old method and $\Delta_{\dot{B}} = 1.18$ for the new method. However, as these misfits are normalized by the level of data error, which is significantly lower in the updated scheme (compare for instance the level of magnetic diffusion in green and data error in red in Fig. 1, secular variation in 2000), this shows that the new method explains a larger part of the data. The change of inversion technique does not affect the large-scale flow pattern, but adds a reasonable amount of small-scale flow complexity, resulting in better compliance with the prior as the posterior misfit for the new inversion is $\Delta_{fs} = 0.88$, in contrast with $\Delta_{fs} = 0.46$ for the old inversion. The impact of explicitly estimating underparametrization and magnetic diffusion is thus arguably beneficial, as it explains more of the data while not dramatically increasing the flow complexity.

The flows obtained with the updated inversion scheme display the same dominant organization in columns parallel to the rotation axis as those previously obtained (see, e.g. fig. 12b in Aubert 2013). A further quantification is provided here by computing the ratio S/A between the energy contained in equatorially symmetric and antisymmetric components of the core surface flow (Fig. 6). The equatorially symmetric part strongly dominates the antisymmetric part, to the point that inverted flows generally show a significantly higher S/A ratios than the prescription of the numerical prior used of the inversion. Similar results have been obtained by Gillet *et al.* (2011), suggesting that the secular variation is best fitted by equator-symmetric flows. Here, such flows consist of a superimposition of convective columns and equator-symmetric thermochemical wind patterns. It is worthwhile noting that the influence of equator-asymmetric thermal mantle control in prior CE diminishes the S/A
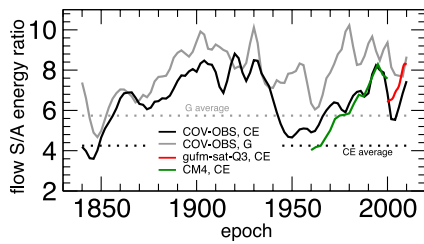
**Figure 6.** Ratio *S/A* of equator-symmetric to equator-antisymmetric component energies in the core surface flows inverted with priors CE, G and geomagnetic field models COV-OBS, gufm-sat-Q3 and CM4. The dotted lines locate the ratio between the average symmetric and antisymmetric energies of the numerical priors.

ratio of inverted flows (compare results with prior CE and prior G), but still yields high equator symmetry.

Figs 7 and 8 present key steps of the flow and magnetic field evolution between 1840 and 2010, inverted using prior CE and geomagnetic field model COV-OBS. From epoch 1870 onwards, the surface core flow (first column) displays a typical conveyor-belt structure with strong, equatorial westward drift beneath the Atlantic, consistent with numerous previous inversions (see review in Finlay *et al.* 2010a). The underlying azimuthal flow (second column) is generally westwards, with eccentric (Pais & Jault 2008; Aubert 2013) shape from 1870 onwards. The core flow evolution is marked by the rapid emergence of strong convective columns most visible around epochs 1914, 1970 and 2006, generally in the Eastern hemisphere (0°E–180°E), suggesting higher activity in this region. These epochs have been identified above as epochs of high secular variation energy at the Earth's surface, and high data misfit $\Delta_{\dot{B}}$ (Fig. 2). The westward eccentric gyre also reflects this behaviour, with localized bursts of westward flows within the main gyre structure at the same epochs. The radial velocity structure (third column) is the superposition of small-scale convective columns and a larger scale hemispherical flow, corresponding to an upwelling in the Eastern hemisphere and a downwelling in the Western hemisphere. Intensity bursts also occur in the radial velocity field at the same epochs and locations as for the azimuthal velocity field and core surface flow. The magnetic field structure
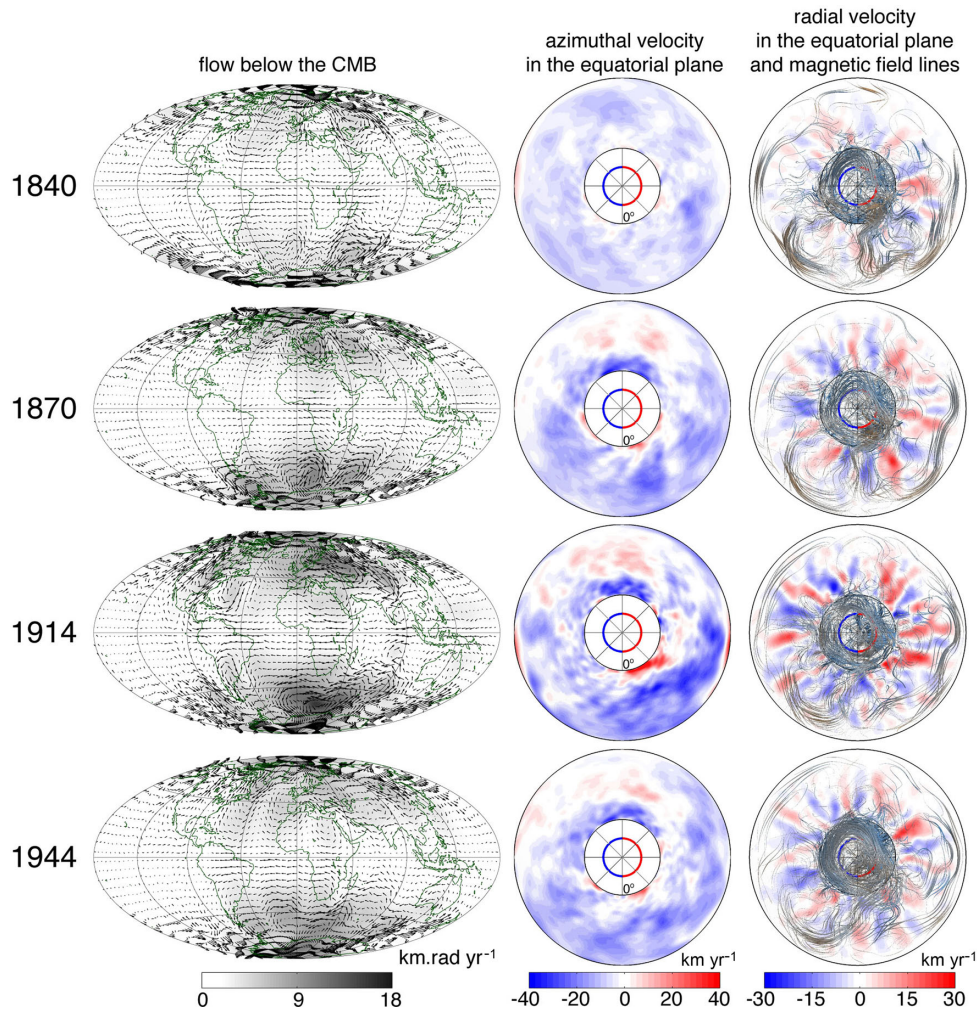
Figure 7. Evolution of flow and magnetic field structures between 1840 and 1944, as imaged from prior CE and the COV-OBS geomagnetic field model. First column: core surface flow (arrows, arbitrary scaling), superimposed on a grey-scale map of the toroidal velocity scalar $T(r_{CMB})$ measuring the amount of local surface rotation. Second column: maps of the azimuthal velocity in the equatorial plane (blue is westwards). The half-circles inside the inner core indicate the orientation of the inner core buoyancy heterogeneity (red is excess buoyancy). Third column: maps of the radial velocity in the equatorial plane (red is outwards), overplotted with a rendering of magnetic field lines where the line thickness is proportional to the local magnetic energy.
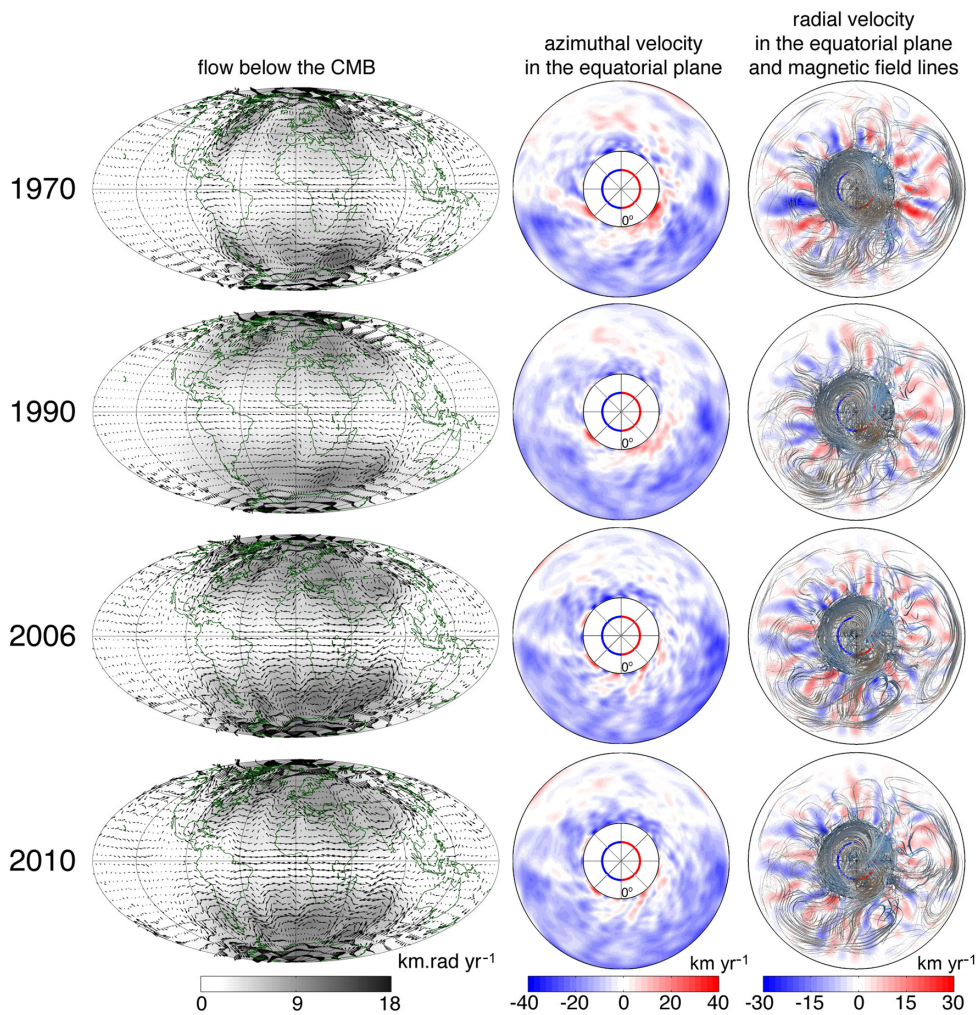
Figure 8. Evolution of flow and magnetic field structures between 1970 and 2010, as imaged from prior CE and the COV-OBS geomagnetic field model (continued from Fig. 7, see figure caption for column definitions).

displays concentrations of azimuthal field at low latitudes, consistent with observations from the direct simulation of the CE model (Aubert *et al.* 2013). These magnetic images show a connexion with the flow upwelling images, with existence of large low-latitude flux tubes beneath the core–mantle boundary in the Eastern hemisphere, where upwelling is broad and strong, and smaller flux loops in the Atlantic hemisphere ($-90°$E to $90°$E), coinciding with the smaller scale vorticity pattern. In the Atlantic hemisphere also, strong radial magnetic flux is found between up- and downwellings, and connects with core–mantle boundary magnetic flux patches at low latitudes, consistently with a mechanism of flux expulsion (Bloxham 1986), where radial motion distorts near-surface azimuthal magnetic flux to form radial flux, which then connects to the surface because of diffusion through the magnetic boundary layer.

Equatorial maps of density anomaly averaged over the last 170 yr are presented in Fig. 9. These maps show a striking hemispherical dichotomy between the Eastern and Western hemispheres, with most of the buoyancy in the east. As such a dichotomy is built into prior CE, it is not surprising to see it emerging as an inversion result. In order to assess the data origin of this pattern, prior G is also used, which does not contain any longitudinal buoyancy heterogeneity. The hemispherical pattern is not sensitive to the change of prior, providing the first observational confirmation that buoyancy
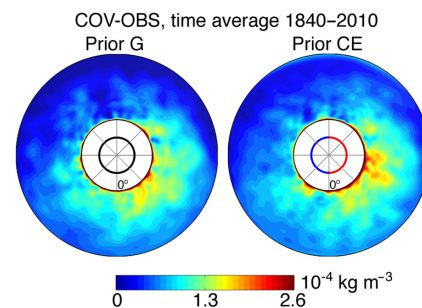
Figure 9. Equatorial maps of convective density anomaly (red is lighter fluid) imaged from model COV-OBS and priors G, CE, and averaged over 1840–2010. When present, the half-circles inside the inner core indicate the orientation of the inner core buoyancy heterogeneity (red is excess buoyancy, a black circle means no inner core buoyancy heterogeneity).

originating from the inner core is higher in the east, corresponding to faster inner core freezing there. This also suggests that convective translation of the inner core should proceed from east to west (if it exists). As already discussed in earlier studies (Aubert 2013; Aubert *et al.* 2013) this conflicts with the hypothesis made in Monnereau *et al.* (2010) and Alboussière *et al.* (2010) but is in agreement with the expected effects of thermal mantle control (Aubert *et al.* 2008).
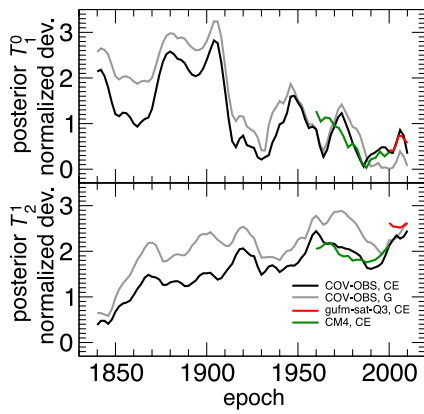
Figure 10. Absolute values of the inverted single-harmonic core surface flow toroidal coefficients $T_1^0(r_{CMB})$ and $T_2^1(r_{CMB})$, normalized by their corresponding standard deviations in the numerical dynamo prior.

The evolution of the surface signature of the eccentric gyre can be further analysed (Fig. 10) by examining posterior normalized deviations for the single-harmonic toroidal flow coefficients $T_1^0(r_{CMB})$ and $T_2^1(r_{CMB})$, respectively, accounting for the westward and eccentric character of the surface conveyor-belt pattern. These are obtained by normalizing the absolute inverted values of these coefficients by the corresponding standard deviations of the numerical dynamo prior, and behave similarly as posterior misfits while focusing on a single harmonic component. The posterior normalized deviation for $T_1^0(r_{CMB})$ shows well-identified peaks centred at 1906, 1948, 1974 and 2006, another indication of the energy surges undergone by the core flow. As mentioned above, these epochs again roughly coincide with surges in Earth surface secular variation energy. No such signal is found in the posterior normalized deviation for $T_2^1(r_{CMB})$, showing that the gyre undergoes rapid fluctuations in its zonal intensity but not in its hemisphericity. A long-term increase in the posterior normalized deviation for $T_2^1(r_{CMB})$ is however clear, which presumably reflects the increase in data quality, and suggests that the absence of eccentricity observed in 1840–1870 (Fig. 7) is a data effect. Posterior normalized deviations for the hemispherical flow $T_2^1(r_{CMB})$ are also generally closer to 1 with prior CE than with prior G, confirming that a buoyancy heterogeneity corresponding to faster inner core growth in the east is beneficial to the reproduction of the eccentric gyre (Aubert 2013; Aubert *et al.* 2013).

An important question is whether the gyre rotates azimuthally due to self-advection, as hypothesized in Aubert *et al.* (2013) in the analysis of the CE model. A rotation of the eccentric gyre is not obvious from Figs 7 and 8, due to fluctuating local anomalies in the gyre. A refined analysis can be performed by defining a gyre centre weighted by the magnitude of the negative azimuthal velocity:

$$\mathbf{r}_G = \frac{\displaystyle\int_S \mathbf{r} u_\varphi (1 - \mathrm{sgn}\, u_\varphi)\mathrm{d}S}{\displaystyle\int_S u_\varphi (1 - \mathrm{sgn}\, u_\varphi)\mathrm{d}S}. \tag{19}$$

Here $\mathbf{r}$, S and u_φ are, respectively, the radius vector, the surface of the equatorial plane and the azimuthal velocity field. Tracking the temporal evolution of the gyre angle, which is defined as the azimuth of $\mathbf{r}_G$, one can assess whether the negative velocity structure moves in the longitudinal direction. Fig. 11 presents the temporal evolution of the gyre angle, obtained with priors G, CE and model COV-OBS. As anticipated, the gyre angle significantly fluctuates with time, but a linear regression gives a long-term trend with drift speed at about $0.1°$ yr^{-1} westwards, fully in line with the drift of $0.12°$ yr^{-1} ($360°$
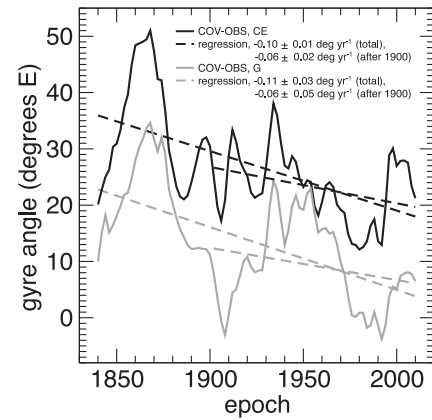
Figure 11. Gyre angle (solid lines, see text) as a function of time, for inversions using priors CE, G and geomagnetic field model COV-OBS. Linear regressions are presented as dashed lines.
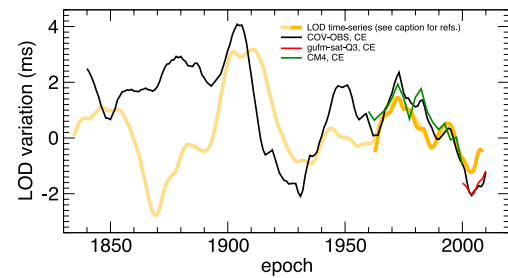
Figure 12. Observed (orange curves) and predicted (other curves, see caption for the prior and geomagnetic field models used) changes in the length of day (l.o.d.) between 1840 and 1990. Two observational models of the l.o.d. are used: LUNAR97 (light orange, spanning 1832–1997, Gross 2001), after removal of a linear trend of 1.7 ms per century and application of a 5-yr running average, and a model for 1958.5–2008.5 (dark orange) constructed by Gillet *et al.* (2009) based on data from Earth Orientation Centre, Paris, and corrected for atmospherical angular momentum variations (see reference for details).

in 3000 yr) obtained in direct simulation of the CE model (Aubert *et al.* 2013). Note again that the observed gyre rotation appears to be fairly robust to a change of prior. If data from the 19th century is rejected, the obtained gyre drift reduces to $0.06°$ yr^{-1} westwards, or half the predicted rate, with a standard error on the order of the drift speed itself in the case of model G.

Observed variations in the length of day (l.o.d.) of core origin can be compared to predictions from the inverted core flows (Jault *et al.* 1988; Jackson *et al.* 1993). Using eqs (25,26) from Aubert (2013) with the same values for the physical constants, the l.o.d. evolution using prior CE is computed in Fig. 12. Results in the observatory era are in line with those of several previous authors [see fig. 5 in Holme (2007) and fig. 9 in Finlay *et al.* (2010a)]: predicted and observed changes in the l.o.d. strongly disagree until 1900, and the sharp observed drop of the observed l.o.d. in 1910 appears to be delayed by about 10 yr, respectively, to the predicted l.o.d. drop. Later in the 20th century, the predicted and observed l.o.d. changes show better synchronization, and the agreement becomes good from 1970 onwards, both in amplitude and shape, although inversions performed with COV-OBS tend to slightly overpredict the l.o.d. changes throughout 1840–2010. As expected, the predicted l.o.d. signal correlates well with the variance pattern of the $T_1^0(r_{CMB})$ normalized core surface flow coefficient (Fig. 10), with sharp l.o.d. drops being located at the epochs identified above of

Table 4. Flow variation timescale τ_{flow} (see text) for flows inverted with prior CE and different geomagnetic field models (first three rows), and for a free direct numerical run of the CE dynamo (last row, velocity field truncated at harmonic degree 30 for consistency with inverted flows). Time derivatives are evaluated by centred finite differences, with spacing between points corresponding to the nodal spacing of the geomagnetic field models, or with an equivalent spacing for the numerical dynamo run (first column). The evaluation of τ_{flow} is performed both for the full velocity field (second column) and for its axisymmetric component (last column).

Model	Spacing (yr)	τ_{flow} (full, yr)	τ_{flow} (axisym., yr)
COV-OBS, CE	2	10.1	18.5
gufm-sat-Q3, CE	0.25	13.0	27.9
CM4, CE	2.5	10.8	22.4
Direct CE run	2	23.7	64.9

rapid intensification of the deep westward flow, particularly after 1910 and after 1970 (Figs 7 and 8).

Having explored the compatibility of the prior model with the main field and secular variation data, it is important to check the ability of this model to correctly account for the secular acceleration of the magnetic field, which does not enter the inversion. Equivalently (Christensen *et al.* 2012), one can look at the variations of the core flow, and more specifically to the flow variation timescale

$$\tau_{\text{flow}} = \sqrt{K_u / K_{\dot u}}. \tag{20}$$

Here, K_u and $K_{\dot u}$ are, respectively, time averages of the kinetic energy of the core surface flow, and of the kinetic energy of its time derivative. As previously shown by Christensen *et al.* (2012), this timescale corresponds to that of low degree magnetic secular acceleration. Table 4 shows that the value $\tau_{\text{flow}} \approx 10$ yr obtained for the inverted core surface flows is on the same order of magnitude as that obtained in a direct numerical run of the CE dynamo model. Note however that τ_{flow} is about twice longer in the numerical run than in the inversions, and three times longer when only the axisymmetric velocity is considered. The reference case in Christensen *et al.* (2012) has parameters similar to the CE dynamo model (although the boundary conditions differ), and yields $\tau_{\text{flow}} \approx 8$ yr, in better apparent agreement with the values of τ_{flow} derived from the geomagnetic field models. Note however that the difference arises from the fact that τ_{flow} in Christensen *et al.* (2012) is computed using the full velocity field spectrum (doing the same here yields $\tau_{\text{flow}} = 12.1$ yr), while the velocity field is truncated here after spherical harmonic degree 30 in order to provide a meaningful comparison with the inverted flows.

4 DISCUSSION

In this study, inverse geodynamo modelling has been extended to provide whole core inversions for the three unknown physical fields characterizing Earth's core dynamics (the velocity, density anomaly and magnetic fields), at single epochs where the main magnetic field, its secular variation and their error statistics are supplied by geomagnetic field models. Concerning the velocity field, a direct estimation of the effects of underparametrization and magnetic diffusion has enabled specification of error levels reduced to the sole observational errors, at the expense of a stronger level of confidence being placed on the prior. This yields sharper core surface flow images (Fig. 5) which explain a larger part of the data while maintaining a level of complexity within the statistical bounds of the prior. The data request highly equator-symmetric core surface flows (Figs 6,

7 and 8), and the deep core flow estimations confirm the presence of largely axially invariant (columnar) flows, superimposed on axially variable, but mainly equator-symmetric thermochemical wind contributions. Furthermore, it has been shown that linear estimation of the deep density anomaly field is best performed as a time average, an averaging time of 170 yr (roughly a convective overturn) appearing sufficient. While the estimations of the velocity and density anomaly fields are supported by robust linear equilibria thought to hold both in the numerical prior model and in the Earth's core, the estimation of the deep magnetic field from its surface signature solely relies on statistical grounds as the linear relation between the two is elusive. This is arguably one of the weaknesses of the updated framework presented here (Table 3), as it is probably more sensitive to a prior change than the inversions for the velocity and density anomaly field.

The compatibility between the data and the prior numerical model, within the error bounds specified for COV-OBS, or prescribed *a priori* for gufm-sat-Q3 and CM4 (Table 2), is generally good, as confirmed by the analysis of prior (Fig. 2) and posterior (Figs 4 and 10) misfits. The fact that such a compatibility is obtained using an admittedly optimistic treatment of errors in the inversion framework reinforces the general confidence that can be placed both in the CE dynamo and in the error specification of the geomagnetic field models, while emphasizing a few areas of significant disagreement: Anomalously high misfits to the magnetic field are witnessed when inverting model COV-OBS at epochs 2000–2010, and high misfits to the COV-OBS secular variation are observed in 1840–1870. Since the CE model manages to provide satisfactory fits at other epochs, this suggests that the corresponding portions of the COV-OBS error covariance matrices may be optimistic.

The temporal evolution of the inverted states provides a coherent, dynamically consistent description of the secular evolution of the geodynamo, and confirms a number of mechanisms observed in a direct run (Aubert *et al.* 2013) of the CE dynamo model. The planetary-scale, eccentric westward columnar gyre appears to be present from 1870 onwards, throughout much of the time span of COV-OBS (Figs 7 and 8). Its absence in the earliest epochs can reasonably be attributed to the large errors initially affecting the data (Figs 1, 3 and 10). Slow westward drift of the gyre itself has been put in evidence (Fig. 11), with a drift speed consistent with the prediction made by the CE dynamo model. Intensity surges in the zonal part of the gyre (Fig. 10) accurately account for observed variations in the length of the day from 1970 onwards (Fig. 12), while the agreement is degraded for earlier epochs, in a way very similar to various results obtained by earlier methods [compare Fig. 12 with fig. 5 in Holme (2007) and fig. 9 in Finlay *et al.* (2010a)].

It is not surprising that inverted deep magnetic field structures (Figs 7 and 8) are similar to those observed in a direct numerical simulation of the CE dynamo model, since they are presumably strongly controlled by the prior. It is nevertheless interesting that they display an apparent dynamic consistency (e.g. magnetic flux winding around vortices) with the inverted flow structures. Also of interest is their azimuthal distribution and how they connect with radial magnetic flux patches at the core–mantle boundary. Low-latitude azimuthal magnetic flux concentrations are present below the core–mantle boundary in the Eastern hemisphere, where they appear to be pushed by the broad core flow upwellings there. In the Atlantic hemisphere, a smaller scale intermingling of columnar vortices and magnetic flux loops containing significant radial flux underlies the equatorial, westward-drifting core–mantle boundary flux patches. This configuration is consistent with the hypothesis

of azimuthal magnetic flux expulsion previously proposed for the physical origin of these patches (Bloxham 1986; Christensen & Olson 2003; Aubert *et al.* 2013).

The 170-yr time-average maps of density anomaly (Fig. 9) highlight a longitudinal hemispheric buoyancy distribution, with significantly higher buoyancy in the Eastern hemisphere. This has been shown not to be an effect of the specification of the CE prior, since a similar map is obtained using an inversion prior without any prescribed longitudinal buoyancy anomaly. This buoyancy distribution is consistent with fast emergence of convective columns predominantly in the Eastern hemisphere (Figs 7 and 8) during phases of intense secular variation. Both results arguably provide strong observational support to faster inner core freezing in the east, possibly as a consequence of thermal mantle control (Aubert *et al.* 2008). Such a configuration likely strongly influences the convective translation of the solid inner core, should the inner core density stratification conditions be favourable to its appearance. In order to be consistent with such a buoyancy pattern, inner core translation should then proceed from east to west. It has also been shown (Fig. 10) that prescribing an inner core buoyancy anomaly compatible with a such translation (as done in the CE dynamo model) improves the inversion fit to the hemispherical part of the core flow. Finally, the imaging reveals a longitudinal phase shift of about $60°$ between the pattern of density anomaly (Fig. 9) and the gyre (Figs 7 and 8), consistent with the kinematics of an hemispherical thermochemical wind.

The inversions show that the CE dynamo model generally correctly accounts for the main field and secular variation data throughout 1840–2010. Concerning the magnetic secular acceleration and the associated core flow variations, it has also been shown (Fig. 4) that the flow variation timescale τ_{flow} deduced from the inversions is on the same order of magnitude as that of a free run of the CE dynamo. This point is interesting because the secular acceleration data are not injected in the inversion, and because the inversion is not regularized in time, meaning that no further dynamic constraint has been applied in addition to the constraints present in the geomagnetic field models used as input. As these constraints are fairly weak in the case of the COV-OBS model, this confirms the earlier suggestion (Christensen *et al.* 2012) that a part of the short timescale variability of the geodynamo is correctly approached by the current generation of numerical simulations. This part presumably relates to convective fluctuations, and other important components of this variability are obviously missing, as witnessed by the fact that τ_{flow} is a few times longer in the numerical model than in the Earth. The scaling analysis presented in eqs (18) and (21) of Christensen *et al.* (2012) suggests that a better match could be obtained from a model with magnetic Reynolds number about twice the value used here. A value $Rm \approx 2000$ is not unrealistic given the recent estimates of the core electrical conductivity (Pozzo *et al.* 2012). Obtaining a better agreement between inverted and simulated values of the flow acceleration timescale however does not necessarily mean that the underlying physics is completely accounted for. Indeed several key timescales in the model are not short enough (Table 1): the Alfvén time is similar to the core overturn time (i.e. too long by a factor 100) and the rotation rate of the planet is on the order of a few years (i.e. too long by a factor 3000 roughly). Bringing these timescales towards more realistic values appears as an important challenge for our understanding of Earth's core dynamics, because the short timescale features presently observed in the inversions have been connected to surges in the Earth surface secular variation energy and because they probably also connect to the mechanism

through which geomagnetic jerks occur (Olsen & Mandea 2007; Chulliat *et al.* 2010). One way of better assessing the part of the geomagnetic signal which is accounted for by the current numerical geodynamo models is to initialize a simulation with an inverted core state from the past, and compare its subsequent forward integration with data and with core states inverted at later epochs. This will be the topic of a forthcoming study. This should enable error quantification for typical forecasts of the future geomagnetic field evolution, and should also provide a basis of reflexion towards simplified modelling strategies that could account for the unexplained part of the signal.

REFERENCES

Alboussière, T., Deguen, R. & Melzani, M., 2010. Melting-induced stratification above the Earth's inner core due to convective translation, *Nature,* **466**(7307), 744–747.

Amit, H., Olson, P. & Christensen, U., 2007. Tests of core flow imaging methods with numerical dynamos, *Geophys. J. Int.,* **168**(1), 27–39.

Aubert, J., 2005. Steady zonal flows in spherical shell dynamos, *J. Fluid. Mech.,* **542,** 53–67.

Aubert, J., 2013. Flow throughout the Earth's core inverted from geomagnetic observations and numerical dynamo models, *Geophys. J. Int.,* **192**(2), 537–556.

Aubert, J. & Dumberry, M., 2011. Steady and fluctuating inner core rotation in numerical geodynamo models, *Geophys. J. Int.,* **184**(1), 162–170.

Aubert, J. & Fournier, A., 2011. Inferring internal properties of Earth's core dynamics and their evolution from surface observations and a numerical geodynamo model, *Nonlinear Process. Geophys.,* **18**(5), 657–674.

Aubert, J., Amit, H., Hulot, G. & Olson, P., 2008. Thermochemical flows couple the Earth's inner core growth to mantle heterogeneity, *Nature,* **454**(7205), 758–761.

Aubert, J., Labrosse, S. & Poitou, C., 2009. Modelling the palaeo-evolution of the geodynamo, *Geophys. J. Int.,* **179**(3), 1414–1428.

Aubert, J., Finlay, C.C. & Fournier, A., 2013. Bottom-up control of geomagnetic secular variation by the Earth's inner core, *Nature,* **502,** 219–223.

Bloxham, J., 1986. The expulsion of magnetic flux from the Earth's core, *Geophys. J. R. astr. Soc.,* **87**(2), 669–678.

Christensen, U.R., 2011. Geodynamo models: tools for understanding properties of Earth's magnetic field, *Phys. Earth planet. Inter.,* **187,** 157–169.

Christensen, U.R. & Aubert, J., 2006. Scaling properties of convection-driven dynamos in rotating spherical shells and application to planetary magnetic fields, *Geophys. J. Int.,* **166,** 97–114.

Christensen, U.R. & Olson, P., 2003. Secular variation in numerical geodynamo models with lateral variations of boundary heat flux, *Phys. Earth planet. Inter.,* **138,** 39–54.

Christensen, U.R., Aubert, J. & Hulot, G., 2010. Conditions for Earth-like geodynamo models, *Earth. planet. Sci. Lett.,* **296**(3–4), 487–496.

Christensen, U.R., Wardinski, I. & Lesur, V., 2012. Timescales of geomagnetic secular acceleration in satellite field models and geodynamo models, *Geophys. J. Int.,* **190**(1), 243–254.

Chulliat, A., Thebault, E. & Hulot, G., 2010. Core field acceleration pulse as a common cause of the 2003 and 2007 geomagnetic jerks, *Geophys. Res. Lett.,* **37,** L07301, doi:10.1029/2009GL042019.

Finlay, C.C. & Jackson, A., 2003. Equatorially dominated magnetic field change at the surface of Earth's core, *Science,* **300,** 2084–2086.

Finlay, C.C., Dumberry, M., Chulliat, A. & Pais, M.A., 2010a. Short timescale core dynamics: theory and observations, *Space. Sci. Rev.,* **155**(1–4), 177–218.

Finlay, C.C. *et al.*, 2010b. International geomagnetic reference field: the eleventh generation, *Geophys. J. Int.,* **183**(3), 1216–1230.

Finlay, C.C., Jackson, A., Gillet, N. & Olsen, N., 2012. Core surface magnetic field evolution 2000–2010, *Geophys. J. Int.,* **189**(2), 761–781.

Fournier, A. *et al.*, 2010. An introduction to data assimilation and predictability in geomagnetism, *Space Sci. Rev.,* **155**(1–4), 247–291.

Fournier, A., Aubert, J. & Thébault, E., 2011. Inference on core surface flow from observations and 3-D dynamo modelling, *Geophys. J. Int.,* **186**(1), 118–136.

Gillet, N., Pais, M.A. & Jault, D., 2009. Ensemble inversion of time-dependent core flow models, *Geochem. Geophys. Geosyst.,* **10,** Q06004, doi:10.1029/2008GC002290.

Gillet, N., Schaeffer, N. & Jault, D., 2011. Rationale and geophysical evidence for quasi-geostrophic rapid dynamics within the Earth's outer core, *Phys. Earth planet. Inter.,* **187**(3–4,SI), 380–390.

Gillet, N., Jault, D., Finlay, C.C. & Olsen, N., 2013. Stochastic modeling of the Earth's magnetic field: inversion for covariances over the observatory era, *Geochem. Geophys. Geosyst.,* **14**(4), 766–786.

Gross, R.S., 2001. A combined length-of-day series spanning 1832–1997: LUNAR97, *Phys. Earth planet. Inter.,* **123**(1), 65–76.

Holme, R., 2007. Large-scale flow in the core, in *Treatise on Geophysics, Volume 8: Core dynamics*, pp. 107–130, ed. Olson, P., Elsevier.

Jackson, A. & Finlay, C.C., 2007. Geomagnetic secular variation and its applications to the core, in *Treatise on Geophysics, Volume 5: Geomagnetism*, pp. 147–193, ed. Schubert, G., Elsevier.

Jackson, A., Bloxham, J. & Gubbins, D., 1993. Time-dependent flow at the core surface and conservation of angular momentum in the coupled core-mantle system, in *Dynamics of the Earth's Deep Interior and Earth Rotation*, Vol. **72,** pp. 97–107, eds Le Mouël, J.-L., Smylie, D.E. & Herring, T., AGU Geophysical Monograph.

Jackson, A., Jonkers, A.R.T. & Walker, M.R., 2000. Four centuries of geomagnetic secular variation from historical records, *Phil. Trans. R. Soc. A,* **358,** 957–990.

Jault, D., 2008. Axial invariance of rapidly varying diffusionless motions in the Earth's core interior, *Phys. Earth planet. Inter.,* **166**(1–2), 67–76.

Jault, D., Gire, C. & Le Mouël, J.-L., 1988. Westward drift, core motions and exchanges of angular momentum between core and mantle, *Nature,* **333,** 353–356.

Lesur, V., Wardinski, I., Hamoudi, M. & Rother, M., 2010. The second generation of the GFZ Reference Internal Magnetic Model: GRIMM-2, *Earth Planets Space,* **62**(10), 765–773.

Lhuillier, F., Aubert, J. & Hulot, G., 2011a. Earth's dynamo limit of predictability controlled by magnetic dissipation, *Geophys. J. Int.,* **186**(2), 492–508.

Lhuillier, F., Fournier, A., Hulot, G. & Aubert, J., 2011b. The geomagnetic secular-variation timescale in observations and numerical dynamo models, *Geophys. Res. Lett.,* **38,** L09306, doi:10.1029/2011GL047356.

Lowes, F. & Olsen, N., 2004. A more realistic estimate of the variances and systematic errors in spherical harmonic geomagnetic field models, *Geophys. J. Int.,* **157**(3), 1027–1044.

Monnereau, M., Calvet, M., Margerin, L. & Souriau, A., 2010. Lopsided growth of Earth's inner core, *Science,* **328**(5981), 1014–1017.

Olsen, N. & Mandea, M., 2007. Investigation of a secular variation impulse using satellite data: the 2003 geomagnetic jerk, *Earth planet. Sci. Lett.,* **255**(1–2), 94–105.

Olsen, N., Mandea, M., Sabaka, T.J. & Toffner-Clausen, L., 2010. The CHAOS-3 geomagnetic field model and candidates for the 11th generation IGRF, *Earth Planets Space,* **62**(10), 719–727.

Pais, M.A. & Jault, D., 2008. Quasi-geostrophic flows responsible for the secular variation of the Earth's magnetic field, *Geophys. J. Int.,* **173**(2), 421–443.

Pozzo, M., Davies, C.J., Gubbins, D. & Alfè, D., 2012. Thermal and electrical conductivity of iron at Earth's core conditions, *Nature,* **485**(7398), 355–358.

Sabaka, T.J., Olsen, N. & Purucker, M., 2004. Extending comprehensive models of the Earth's magnetic field with Oersted and CHAMP data, *Geophys. J. Int.,* **159**(2), 521–547.